

MATERIALS SCIENCE

Unveiling the microscopic origin of anomalous thermal conductivity in amorphous carbon

ZhongTing Zhang^{1†}, Jian Luo^{2†}, HengAn Wu¹, Hao Ma^{2*}, YinBo Zhu^{1*}

Amorphous carbons pose fundamental questions, including incomprehensible phase transformations, microtopology identification, and origins of anomalous properties. However, transition pathways from low-density, high- sp^2 structures to high-density, high- sp^3 forms remain poorly understood, within which thermodynamical behaviors are practically unexplored. Here, we investigated the phase transition and thermal transport properties of a recently reported amorphous carbon phase, amorphous diaphite (a-DG). The continuous transformation pathway of a-DG is characterized by distinctive heterogeneous microstructural evolutions across a wide density range. We observed anomalous thermal conductivities in a-DG, which initially decrease and then increase with the density and sp^3/sp^2 ratio, deviating markedly from previously reported trends. This anomaly originates from changes in phonon mean free path and phonon lifetime at the medium-frequency range (7 to 30 terahertz), dictated by the unique two-stage microtopological transition. These findings challenge conventional views of thermal conductivity in amorphous carbons, and, in a wider context, our mechanistic understanding provides fundamental insights into phase transitions and thermodynamic mechanisms of other amorphous materials.

INTRODUCTION

Carbon, a common yet mystical material, continues to reveal groundbreaking microstructures and distinctive properties (1–4). In the past decades, amorphous carbons have garnered broad attention for their intriguing microtopologies and unique physical characteristics, ranging from monolayer to three-dimensional (3D) blocky amorphous structures (4–19). The monolayer phases, dominated by sp and sp^2 hybrid bonds, exhibit pronounced anisotropy in mechanical, thermal, and other physical properties between in-plane and cross-plane directions (5–9). Liu and coworkers (8, 9) have reported the synthesis and property modulation through disorder tuning of monolayer amorphous carbon, highlighting their profound potential to advance our understanding of the structure-property relationship in amorphous materials. In contrast, blocky amorphous carbons encompass a broad spectrum of densities and hybridization states, with diverse microtopologies and textures that critically influence their thermal and mechanical behaviors (4, 10–25). Low-density blocky amorphous carbons, such as glassy carbon (GC) and pyrolytic carbon (PyC), display markedly distinct microscale textures (11, 23, 26). PyCs usually feature 3D connectivity and high graphitization, characterized by disordered graphene network (DGN) with medium-range ordered (MRO) microstructures (4, 13, 23, 26, 27). Recent experiments under high-pressure and high-temperature (HPHT) conditions have enabled the synthesis of several high-density tetrahedral amorphous carbons (ta-Cs), marked by sp^3 -rich hybridizations and notable atomic disorder (10–12, 16–22, 28–31). Atomically disordered diamonds with densely packed amorphous regions were synthesized (12, 19, 20), giving rise to metastable phases like paracrystalline diamond and amorphous diaphite (a-DG) (18, 20, 21, 32). Extensive nucleation and growth of nanocrystalline diamond grains

were observed within the high-density amorphous matrix under extreme conditions (12, 18, 20). Amorphous carbons have demonstrated exceptional mechanical properties compared to their crystalline counterparts. The continuous discovery of groundbreaking microtopologies and phase transition pathways is enriching the microstructural landscape of amorphous carbons, expanding their potential applications.

Beyond their complex microstructures and unusual mechanical performance, amorphous carbons have also garnered substantial research interest concerning thermal transport behaviors and phonon mechanisms (20, 22, 33–37). Unlike most other amorphous materials, amorphous carbons exhibit a remarkably wide range of thermal conductivity (~ 0.1 to $\sim 37 \text{ W m}^{-1} \text{ K}^{-1}$) (20, 22, 33, 37), primarily due to their broad variations in density, sp^3/sp^2 hybridization degrees, and diverse microtopologies. The density and sp^3/sp^2 ratio are widely recognized as primary determinants of thermal conductivity, influencing both phonon-like and diffusive vibrational modes (35–38). However, most studies have reported a simplified, monotonic relationship between thermal conductivity, density, and sp^3 hybridization degree in amorphous carbons (33–42). For instance, low-density amorphous carbons, such as sp^2 carbon films and foams, typically exhibit low thermal conductivities (34, 37, 38), attributed to their highly disordered microtextures that enhance phonon scattering and impede thermal transport. In contrast, high-density amorphous carbons, such as sp^3 -hybridized ta-Cs and nanodiamonds (NDs), demonstrate markedly higher thermal conductivities (20, 35–37, 40) due to extended phonon mean free paths (MFPs) facilitated by local MRO nanocrystalline structures (20). Beyond density and hybridization, microtopologies and textures have a more direct impact on thermal transport. High-order structures such as PyCs and graphite, despite their relatively low density, often exhibit ultrahigh in-plane thermal conductivities (33, 43). At the extreme end, diamond—a purely sp^3 -hybridized crystalline material—achieves the highest thermal conductivity, reaching $\sim 2000 \text{ W m}^{-1} \text{ K}^{-1}$. However, a knowledge gap persists in understanding the transitional regions bridging low-density graphene-like and high-density diamond-like structures. Numerous intricate metastable phases were unveiled within this transitional region (4, 11, 24, 28, 44), characterized by continuous

¹CAS Key Laboratory of Mechanical Behavior and Design of Materials, Department of Modern Mechanics, University of Science and Technology of China, Hefei 230027, China. ²CAS Key Laboratory of Mechanical Behavior and Design of Materials, Department of Thermal Science and Energy Engineering, University of Science and Technology of China, Hefei 230027, China.

*Corresponding author. Email: mhao@ustc.edu.cn (H.M.); zhu Yinbo@ustc.edu.cn (Y.Z.)

†These authors contributed equally to this work.

evolution of density and sp^3/sp^2 hybridization but notable discontinuous thermal transport behaviors, especially between the various ordered/disordered structures at low densities. Because of the intricate and poorly tunable microtopologies and textures, current research has yet to elucidate the transition pathways from graphite-like to diamond-like configurations, and the role of microstructural ordering in thermal transport within this transitional region remains largely unexplored.

The existence of multiple phases in the transition region from low-density to high-density amorphous carbons has been revealed by recent simulations and experiments (4, 11, 24, 28, 44), especially highlighting the pronounced discontinuity in microtopological features at similar densities and sp^3/sp^2 ratios (4, 15). Recently, Li, Tian, and coworkers reported a unique C/C composition of ND embedded within disordered multilayer graphene (DMG) (4, 21, 45). Under HPHT conditions, GC precursors transformed into the sp^2 - sp^3 hybrid ND-DMG through the nucleation and diffusion-driven growth of sp^3 hybridized amorphous and ND grains (21). Meanwhile, the nanometer-sized curved graphene fragments developed into a disordered 3D network of graphene nanosheets within the sp^2 -hybridized DMG phases, having enhanced graphitization and better continuous 3D connectivity (21). Our simulations have shown that the intricate amorphous phases and coherent/incoherent interfaces create complex energy barriers and local minima, resulting in the formation of a series of metastable heterogeneous amorphous phases during this phase transformation process (4, 45). These heterogeneous metastable phases were designated as a-DG. Unlike other amorphous carbons, a-DG features more pronounced short- and medium-range ordered (SMRO) microtopologies arising from the 3D network of graphene nanosheets and nano-sized diamond nuclei, encompassing a wide range of densities. This unique microstructure enables the establishment of a continuous transition pathway from graphene-like to diamond-like amorphous carbons (4, 15, 45). As a result, a-DG holds promise for bridging the gap between the two high-thermal conductivity extremes within the density transition region and providing a more comprehensible understanding of the role of microstructure ordering in thermal conductivity for amorphous carbons.

In this study, we investigated the phase transformation pathway and thermal transport property of a-DG with varying densities (2.36 to 3.18 g cm⁻³) using large-scale molecular dynamics (MD) simulations. We uncovered a continuous phase transformation pathway from the sp^2 -hybridized DMG to sp^3 -hybridized ND, characterized by a series of metastable heterogeneous a-DGs. Notably, a-DGs display a distinctive thermal conductivity dependence on density and sp^3 hybridization degree, whose thermal conductivities initially decrease and then increase with density and sp^3 hybridization, deviating markedly from previously reported trends that thermal conductivity monotonically increases with density and sp^3 hybridization. This anomalous thermal conductivity trend stems from the evolution of phonon lifetimes at the medium-frequency range of 7 to 30 THz through the unique heterogeneous two-phase microtopology transition, marking a pronounced departure from other amorphous carbons. By focusing on the continuous transition pathway from graphene-like to diamond-like amorphous carbons with SMRO, our findings successfully demonstrate the tunability of microstructural ordering and provide fundamental insights into its critical role in determining thermal conductivity.

RESULTS

Phase transformation of a-DG

In the beginning, we investigated the phase transformation pathway between sp^2 -hybridized DGN and sp^3 -hybridized ND. Starting from DGN precursors (13, 27, 45), a-DGs with varying densities (2.36 to 3.18 g cm⁻³) and hybridization states were generated via a pressure-induced phase transformation process (Fig. 1). These transformations were modeled using the environment-dependent interatomic potential (EDIP) (46), with additional simulation details provided in the Materials and Methods and the Supplementary Materials. EDIP has demonstrated considerable efficiency in simulating the microstructures and physical-mechanical properties of various kinds of amorphous carbons (4, 13, 15, 27, 32, 34, 45). As shown in Fig. 1A, atomic models of a-DGs at different densities illustrate the microtopology evolution along the phase transformation pathway, highlighting distinctive heterogeneous microtopologies. Low-density structures (e.g., 2.36 g cm⁻³) feature a disordered 3D network of graphene fragments (green atoms) with high graphitization and continuous connectivity. The pressure-induced transformation process involves two stages (45), amorphization and crystallization, with a transition boundary at 20 GPa (fig. S1A). In the amorphization stage, atomically disordered regions (white atoms in Fig. 1A) emerge and expand at topological defects within the DGN as the density increases, leading to an increase in potential energy (fig. S1A). Further pressurization promotes the formation of numerous nucleation sites for ND grains (blue and orange atoms) within the extended amorphous regions. This rapid nucleation and growth of ND grains result in decreased potential energy (fig. S1A) and the development of coherent and incoherent interfaces between DMG and ND phases (4, 45). The simulated a-DG models exhibit slightly lower sp^3 hybridizations compared to other amorphous carbon phases of similar density as shown in fig. S1B (4, 35–37, 45). This is attributed to the presence of multilayer graphene fragments with SMRO microtopologies and fewer topological defects, consistent with recent simulations (4, 45).

Then, the structural transition process is further illustrated by simulated transmission electron microscopy (TEM) images in Fig. 1 (B and C) and fig. S4, where “G” denotes DMG fragments and “D” represents ND grains. These microtopologies and the numerous graphene-like/diamond-like interfaces align closely with recent experimental observations (21, 28). Moreover, the x-ray diffraction (XRD) patterns in Fig. 1D, alongside the angular distribution function (ADF) and radial distribution function (RDF) in fig. S2, confirm a continuous phase transformation from a graphitized state to a diamond-like crystallized state. The two arrows in Fig. 1D and fig. S3 (A and B) indicate the evolution and shifts in diffraction peaks of our simulated XRD patterns, aligning with structural changes observed in related experiments (21), as shown in fig. S3 (C and D). In addition, the leftward shift of ADF peaks (fig. S2, A and C) reflects hybridization conversion from sp^2 dominated to sp^3 dominated, while the rightward shift of RDF peaks (fig. S2, B and D) corresponds to the longer bond distances of sp^3 bonds compared to sp^2 bonds. Furthermore, the simulated TEM images of high-density a-DG (3.09 g cm⁻³; fig. S4, A to C) exhibit strong consistency with the experimental images DMG-ND samples (21) in fig. S4 (D and E), supporting the reliability of our structural models and phase transition analysis. These comprehensive microstructure characterizations elucidate the continuous phase transformation pathway linking sp^2 -hybridized DMG with sp^3 -hybridized ND.

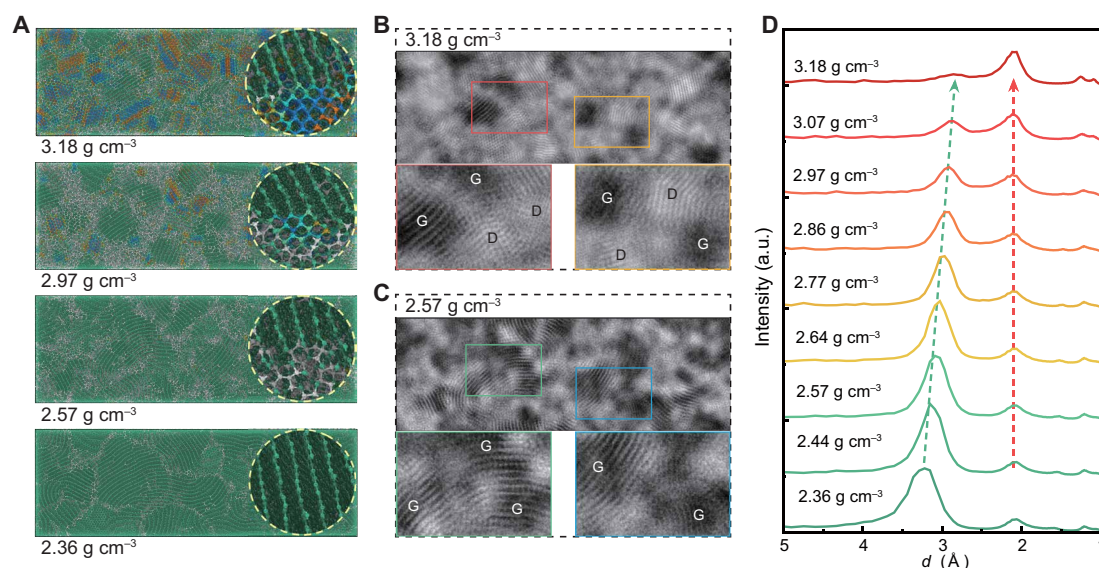


Fig. 1. Microtopology and phase transition of a-DG. (A) Atomic models of a-DG at various densities (45), showcasing heterogeneous microstructures characterized by a heterogeneous two-phase composite topology consisting of DMG and ND phases. Insets illustrate the phase transformation process: sp^2 -hybridized graphene fragments (green atoms) transition into sp^3 -hybridized amorphous tetrahedral carbon (white atoms), which subsequently crystallize into ND (blue and orange atoms). This transformation results in numerous coherent and incoherent interfaces between DMG and ND. (B and C) Simulated TEM images of two a-DG models with densities of 3.18 and 2.57 $g\ cm^{-3}$, respectively. In simulated TEM images, G denotes DMG fragments, while D represents ND grains. The microtopologies and abundant interfaces between DMG and ND observed in (A) to (C) align closely with recent experimental findings (27, 28). (D) XRD patterns of a-DG at various densities, illustrating the phase transformation. The arrows indicate the shift in diffraction peaks, reflecting structural changes that align with observations from related experiments (21). a.u., arbitrary units.

Although the EDIP primarily governed the phase transformation simulations, the stability of the a-DG models was also verified using the neuroevolution potential (NEP), a state-of-the-art machine learning force field (47). Covering a wide range of amorphous carbon configurations with different bonding modes and structural heterogeneity (47, 48), NEP has demonstrated exceptional capability in simulating topological microstructures and physical properties, including thermal and phonon transport properties, across a wide range of amorphous carbons (36, 37, 49–51). Furthermore, it also exhibits strong generalizability, having been successfully applied to a broad range of applications, including the simulation of spectroscopy and polarizability properties, materials interfaces, mechanical responses, phase transitions, and so forth (48). The reliability of NEP with respect to experimental observations has also been validated in previous studies through comparisons with experimental results (48). In our simulations, the a-DG models described by NEP exhibited structural characteristics identical to those derived from EDIP, including ADF, RDF, and XRD patterns (figs. S2 and S3). Moreover, both force fields yielded similar sp^3 hybridization fractions and crystallinities (Fig. 2A), underscoring NEP's effectiveness in modeling the intricate heterogeneous composite structures of a-DGs. For thermal transport properties, such as volumetric heat capacity (C_v) and phonon density of states (PDOS), NEP demonstrated superior accuracy compared to EDIP, as shown in Fig. 2 (B to D). Specifically, C_v calculated using EDIP showed an initial increase followed by a decrease, whereas C_v derived from NEP increased monotonically with density. This trend is consistent with the expectation that C_v should rise with density due to the lower specific heat capacity of graphene (52) compared to diamond (53). Hence, NEP is considered more reliable than EDIP for C_v calculations. In addition, the maximum phonon frequency of the PDOS

calculated with EDIP exceeded 60 THz (Fig. 2C). However, on the basis of the phonon frequencies of diamond (54, 55) and graphite (56, 57), the expected maximum phonon frequency for a-DGs should be around 50 THz, as calculated by NEP (Fig. 2D). Despite these differences, both force fields exhibited similar phonon peak shifts (Fig. 2, C and D). The trends in C_v and PDOS shown in Fig. 2 (B to D) underscore the accuracy of NEP in simulating the thermal transport properties of a-DGs. Considering the relatively insufficiency of EDIP in describing C_v and PDOS as illustrated in Fig. 2, all the subsequent simulation results of thermal transport behaviors presented in this study are based on NEP.

Anomalous thermal transport behavior

Next, we focused on the thermal transport behaviors of a-DGs along the phase transition pathway from GC to DMG/ND. Our calculated classical (green stars) and quantum-corrected (red stars) thermal conductivities of a-DGs averaged across three directions are compared to previously reported amorphous carbons (solid and hollow markers) in Fig. 3 and fig. S5 (see the simulation details provided in the Materials and Methods) (20, 33–42, 58, 59). The quantum-corrected thermal conductivity (60, 61) in a-DGs is observed to be nearly half of the classical thermal conductivity while showing better agreement with experimental results (hollow markers), consistent with previous studies (36, 37). However, unlike previous studies that consistently demonstrated a monotonic increase in thermal conductivity with density (Fig. 3A), a-DGs exhibit an anomalous density-dependent behavior. Specifically, the thermal conductivity in a-DGs initially decreases, reaching a local minimum at a density of $\sim 2.9\ g\ cm^{-3}$, followed by an increase as the density continues to rise. On the other hand, hybridization states are widely recognized as critical determinants of thermal conductivity in amorphous carbons (35). Previous

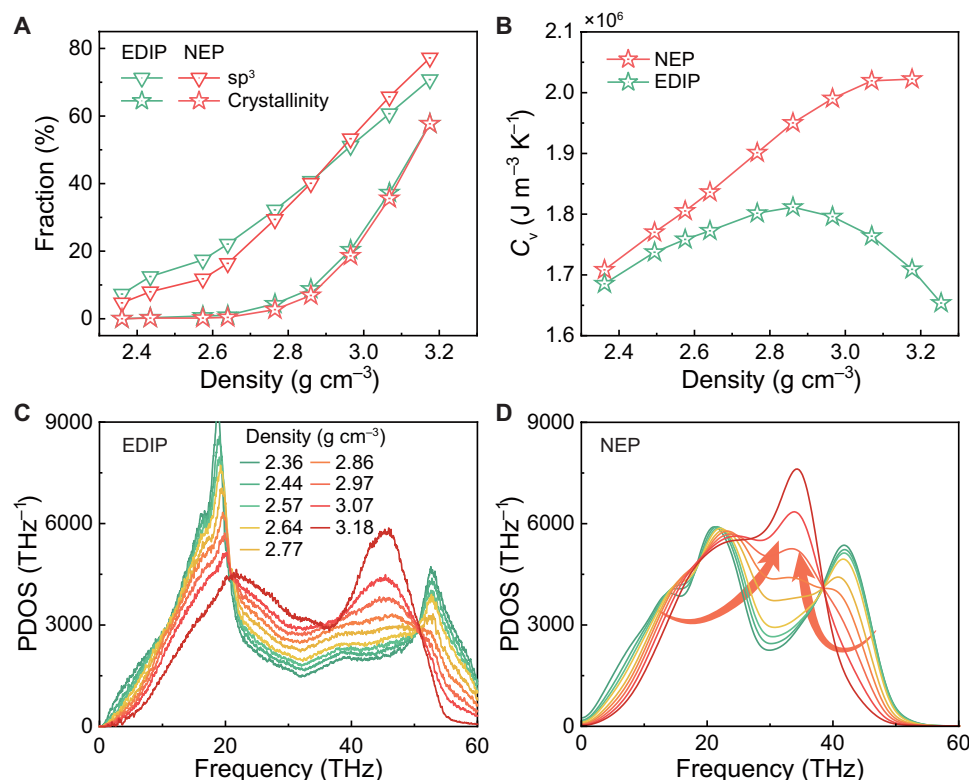


Fig. 2. Comparison of effectiveness between EDIP and NEP. (A) The sp³ ratio and crystallinity calculated using both force fields exhibit similar trends, indicating the effectiveness of both EDIP and NEP in stabilizing a-DG structures. (B) Volumetric heat capacity (C_v) calculated using NEP demonstrates superior accuracy compared to EDIP, with NEP showing a consistent monotonic increase in C_v with density. (C and D) PDOS of a-DGs, calculated via EDIP (C) and NEP (D). The rational maximum phonon frequency and the shift of PDOS peaks marked by red arrows reveal that NEP provides more accurate phonon properties, aligning better with expected maximum phonon frequencies and shifts based on experimental data.

reports (solid symbols in Fig. 3B) have highlighted a positive correlation between thermal conductivity and the sp³/sp² hybridization ratio (36, 37). However, the a-DGs deviate from this trend, displaying a nonlinear dependence on hybridization (red stars in Fig. 3B), underscoring their distinctive anomalous thermal transport behavior. Besides, we also noted that the thermal conductivity of a-DGs showcases several interesting characteristics. In addition to the distinct thermal conductivity trend compared to other amorphous carbons, the thermal conductivity at different densities tends to stabilize (pink-striped region in Fig. 3A), resulting in relatively high thermal conductivity at low densities. This property, combined with its exceptional hardness and other superior mechanical properties (21), presents potential for applications such as in high-performance thermal interface materials.

Microtopological origin for the anomaly

The quantum-corrected thermal conductivity of a-DGs as a function of sp³ hybridization is shown in Fig. 4A, highlighting three representative phases (I, II, and III). Despite minor anisotropy, as shown in fig. S6A, the average thermal conductivities of a-DGs exhibit an anomalous dependence on sp³ hybridization. Thermal conductivity decreases from phase I to II, reaches a turning point at II, and then increases from II to III. In addition, sp³ hybridization increases almost linearly with density, while crystallinity follows a two-stage pattern (45): a slow increase between 2.36 and 2.86 g cm⁻³, followed by a sharp increase above 2.86 g cm⁻³, as depicted in

Fig. 4B. These differences cause a notable delay between sp³ hybridization and crystallinity (45), contributing to the heterogeneous two-stage evolution of microtopologies illustrated in Fig. 4C. In the first stage (I to II), atomically disordered regions (white atoms) emerge and expand through an amorphization process, during which sp³ hybridization increases steadily while crystallinity remains relatively unchanged. In the transition from II to III, numerous diamond grains (blue and orange atoms) nucleate within the amorphous regions, substantially enhancing crystallization.

It is worth noting that the anomalous trend of thermal conductivities in Fig. 4A is intrinsically linked to this microtopology evolution as the density varies. The DGN precursor (I) in Fig. 4 (C and D) consists of a disordered 3D network of graphene fragments, characterized by high graphitization and continuous connectivity, which exhibits MRO microstructures. Similar to PyCs, these semi-ordered topologies can enhance phonon transport, leading to relatively high thermal conductivity at low densities. As the system transitions from I to II, the presence of various defects and distortion of microstructures within the amorphous regions critically increase phonon scattering and impede phonon transport, contributing to a marked reduction in thermal conductivity. However, with further crystallization, the induced ND grains with MRO effectively suppress phonon scattering and facilitate phonon transport, resulting in increased thermal conductivities at high densities. Rather than a simple variation in composite composition with predictable properties, the structural evolution of a-DGs represents a distinct phase transition

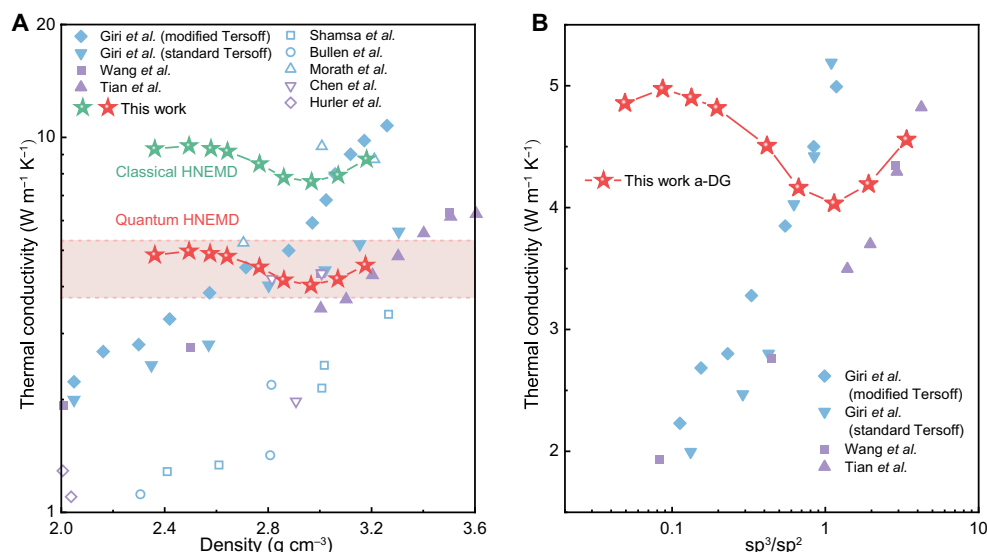


Fig. 3. Computed thermal conductivity of a-DGs. The comparison of thermal conductivity between a-DGs (red and green stars) and other amorphous carbons (solid and hollow scatters) as a function of density (A) and hybridization (B). The red and green stars indicate the quantum-corrected and classical thermal conductivity of a-DGs, calculated using the homogeneous nonequilibrium molecular dynamics (HNEMD) method with NEP, averaged across three directions. The solid and hollow scatters represent computational (35–37) and experimental thermal conductivities (38–42) for previously reported amorphous carbons. Here, we show quantum-corrected thermal conductivity by Moon and Tian (36) and Wang *et al.* (37). See fig. S5 for more other reported thermal conductivity. In (A), the density dependence of thermal conductivity in all previously reported amorphous carbons is monotonic, while a-DGs exhibit an anomalous density dependence of thermal conductivity. In (B), apparent positive correlations between thermal conductivities and the sp^3/sp^2 hybridization ratio in previously reported amorphous carbons highlight the critical role of hybridization in determining thermal conductivities. However, the anomalous thermal conductivity of a-DGs (red stars) is characterized with substantial nonlinear dependence on hybridization.

process from GC to the ND/DMG composite, during which the sp^2 -hybrid DGNs break down into sp^3 -hybrid amorphous regions that provide nucleation sites for the further formation and growth of ND grains. This phase transition behavior leads to an innovative anomalous thermal conductivity evolution that has not been observed in any other amorphous carbons or amorphous materials. The interplay between thermal conductivity and microtopologies underscores the complexity of thermal behavior in a-DGs, establishing a foundation for a more in-depth exploration of thermal transport mechanisms in subsequent sections.

Phonon transport mechanisms

Last but not least, the ADF and RDF for three representative phases (I, II, and III in Fig. 4) of a-DGs are presented in Fig. 5A. Phases I and III exhibit sharper peaks in both ADF and RDF compared to phase II, indicating more pronounced SMRO microtopologies. The shifts in peak positions further highlight the distinctive structural transition. On the basis of the phonon gas model, lattice thermal conductivity (κ) is expressed as $\kappa \propto C_v v_g^2 \tau$, where v_g is the phonon group velocity, τ is the phonon lifetime, and $\lambda = v_g \tau$ is the phonon MFP. As shown in Fig. 2B, C_v is proportional to density. To isolate the impact of C_v , thermal diffusivity ($\alpha = \kappa / C_v \propto v_g \lambda$) is extracted and presented in Fig. 5B, revealing a similar trend to κ as the density increases. The phonon group velocities (v_g) extracted from the current correlation function (62, 63) are shown in Fig. 5 (C and D). Both longitudinal and transverse group velocities exhibit an upward trend with increasing density in Fig. 5C, attributed to the enhanced sp^3 hybridization, which leads to greater bond stiffness. Given the similar thermal conductivity trends observed along all three directions (x , y , and z), the x direction is selected as a

representative example for subsequent calculations of thermal and phonon properties.

Notably, as the structure undergoes transition with the increasing density, the PDOS peaks (Fig. 2D) exhibit a tendency to converge toward the center, aligning well with the previous findings (64). Specifically, the PDOS peaks at low frequency (~ 20 THz) and high frequency (~ 45 THz) shift to medium frequency (~ 30 THz) as marked by red arrows, indicating an increase in the population of phonons at the medium frequencies and a transition from a graphene-like to a diamond-like structure (65, 66). Quantum-corrected spectral κ_x in Fig. 5E reveals a migration of peaks. During the transition from phase I to II, phonon contributions across all frequency ranges, particularly within 7 to 30 THz, are markedly suppressed because of the decreased structural order. As the system transforms from phase II to III, contributions from low-frequency phonons (7 to 15 THz) are notably reduced, while those from medium-frequency phonons (15 to 30 THz) are substantially enhanced. This shift in phonon contributions reflects a **two-stage microtopology transition**. Initially, thermal conductivity **decreases** as the overall phonon contributions decline **because of the disorder** introduced by microstructural defects (**phase I to II**). Subsequently, thermal conductivity increases as medium-frequency phonons (15 to 30 THz) contribute more substantially during the **further phase transition** (phase II to III).

The normalized cumulative κ_x in Fig. 5F indicates that phonons in the frequency range of 7 to 30 THz account for $\sim 75\%$ of the total thermal conductivity, with these phonons having a MFP below 6 nm, as shown in Fig. 5G. The MFP for phonons in the 3- to 30-THz range as a function of density is profiled in Fig. 5H. The MFP within the 7- to 30-THz range follows the same trend as thermal conductivity—initially decreasing and then increasing—indicating the **dominant**

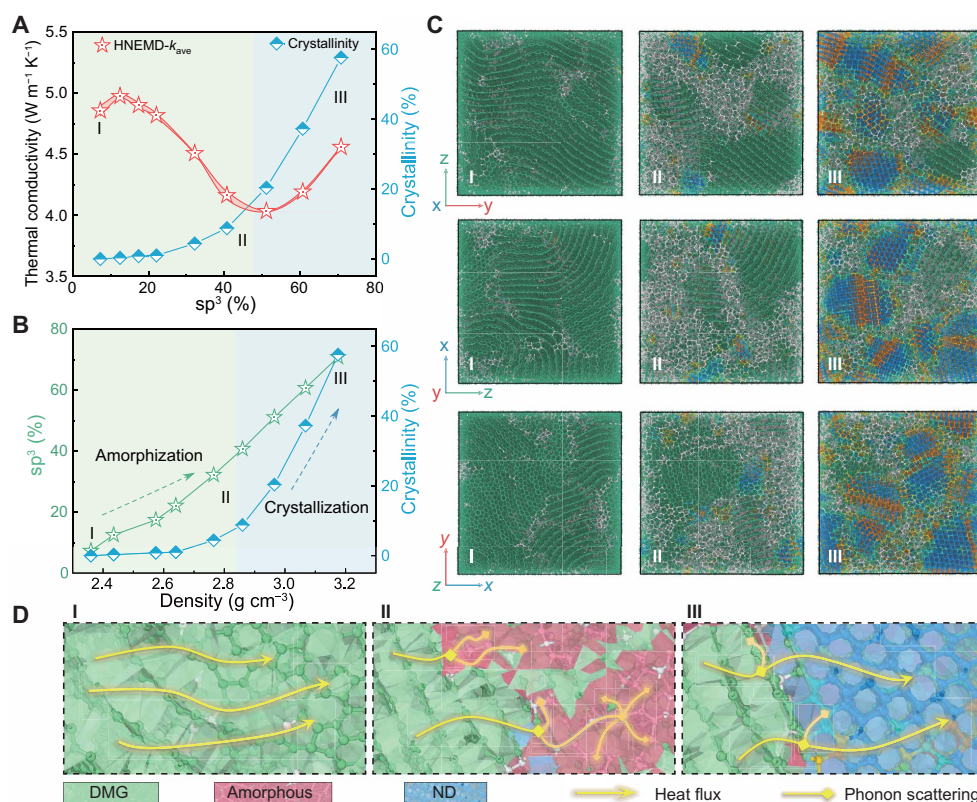


Fig. 4. Microtopology dependence on thermal conductivities in a-DGs. (A) The average quantum-corrected thermal conductivities and crystallinity as a function of sp^3 hybridization. The thermal conductivities exhibit an anomalous dependence on sp^3 hybridization, decreasing from I to II, followed by a turning point at II and an increase from II to III. (B) Density dependence of sp^3 hybridization and crystallinity, where the crystallinity demonstrates a considerable delay compared to the sp^3 hybridization as the density increases. (C and D) Illustrations and schematic diagrams of the microtopology evolution for three representative phases (I, II, and III) with densities of 2.36, 2.86, and 3.18 g cm^{-3} . From top to bottom in (C), each row depicts the yz-, zx-, and xy-plane plots, respectively. The anomalous trend in (A) is intrinsically ascribed to the microtopology evolution as density varies. The DGN precursor (I) comprises MRO microstructures of graphene-like fragments (green atoms), which could enhance phonon transport efficiency, thereby leading to the relatively high thermal conductivity at low densities. The various defects and distortion of microstructures in amorphous phases (white atoms in II) could severely increase phonon scatterings and hinder phonon transport, resulting in the decreased thermal conductivity as the density increases. With further crystallization, the induced ND grains (blue and orange atoms) with medium-range order could suppress the phonon scatterings and facilitate phonon transport, prompting the increased thermal conductivities in higher densities (III).

role of MFP within this frequency range in governing the thermal conductivity of a-DGs. Furthermore, the MFP has also demonstrated a distinctive negative correlation with the proportion of amorphous atoms during phase transformation. As depicted in fig. S6B, structures with low sp^3 content (green scatters) exhibit higher MFPs, attributed to the presence of graphene-like fragments with relatively better SMRO. During the amorphization process (green arrow), a temporal mismatch emerges between the evolution of sp^3 content and crystallinity, leading to an increased proportion of amorphous regions in the intermediate structures (yellow scatters in fig. S6B). These amorphous regions severely hinder phonon propagation, resulting in a considerable reduction in MFP. In the subsequent crystallization stage (red arrow), the conversion of amorphous regions into ND grains enhances phonon transport, thereby increasing the MFP. Given the upward trend of ν_g with increasing density in Fig. 5E, the nonmonotonic behavior of the 7- to 30-THz MFP (initially decreasing and then increasing) is attributed to variations in phonon lifetime rather than group velocity. In other words, the anomalous thermal conductivity in a-DGs is primarily driven by the evolution of phonon MFP and lifetime within the medium-frequency

range of 7 to 30 THz, governed by the unique two-stage microtopology transition.

DISCUSSION

We here illustrate the phase transformation pathway and thermal transport properties of a-DGs with densities ranging from 2.36 to 3.18 g cm^{-3} . Through comprehensive microstructure characterizations, a continuous phase transformation pathway linking sp^2 -hybridized DMG and sp^3 -hybridized ND was elucidated, revealing a two-stage microtopologies transition. The a-DGs exhibit relatively low sp^3 hybridizations compared to other amorphous carbons at similar densities, due to the presence of multilayer graphene fragments with SMRO microtopologies and fewer topological defects. An anomalous behavior in thermal conductivity was observed in a-DGs, characterized by an initial decrease followed by an increase as density and the sp^3 hybridization increase. This behavior is distinct from previous observations in all the other amorphous carbon phases where thermal conductivity monotonically increases with the density and sp^3/sp^2 hybridization ratio, which is typically

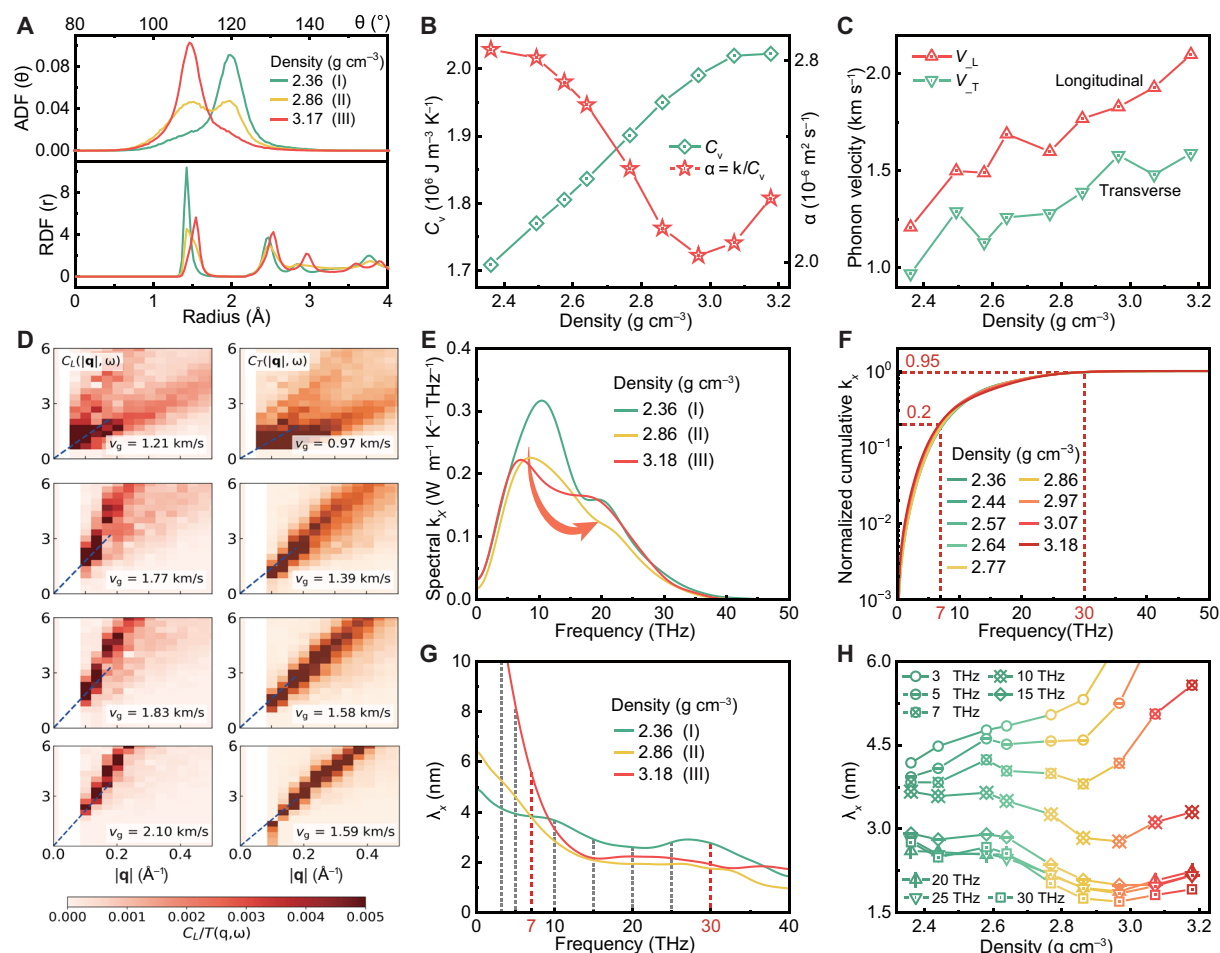


Fig. 5. Phonon properties of a-DGs. (A) The ADF and PDF of the three representative phases (I, II, and III). (B) The volumetric heat capacity (C_v) and thermal diffusivity ($\alpha = \kappa/C_v$) as functions of density. Here, α shows a consistent trend with κ , indicating that C_v is not a dominant factor in determining the nonmonotonic behavior of κ . (C) The phonon group velocity as a function of different densities, extracted from (D) the current correlation function, which is presented as a function of wave vector \mathbf{q} and vibrational frequency. The current correlation functions of four representative densities of 2.36, 2.86, 2.96, and 3.17 g cm^{-3} are illustrated in (D). (E) The spectral thermal conductivity along the x direction (κ_x) as a function of phonon frequencies. The peaks shift from low frequency (~ 10 THz) to medium frequency (~ 25 THz). (F) The normalized cumulative thermal conductivity in the x direction (κ_x) for a-DGs with different densities, showing that about 75% of the total thermal conductivity is contributed by phonons with frequencies of 7 to 30 THz. (G) The phonon MFP along the x direction (λ_x) as a function of phonon frequency. (H) The λ_x as a function of density for different frequencies in the range of 3 to 30 THz and λ_x in the range of 7 to 30 THz exhibits a trend similar to κ_x , suggesting that phonon MFP at 7 to 30 THz is a dominant factor in the variation of thermal conductivity with density.

considered a determining factor for thermal conductivity. While all previous studies reported a simplified, monotonic relationship between thermal conductivity, density, and sp^3 hybridization degrees in amorphous carbons (34–42), we uncovered an innovative anomalous thermal conductivity evolution with density and sp^3 hybridization degrees due to changes in the phonon MFP and phonon lifetime at the medium-frequency range of 7 to 30 THz, which was correlated with the unique two-stage microtopological transition. Specifically, in the first stage (I to II), the presence of various defects and distortion of microstructures within the amorphous regions critically increase phonon scattering and reduce phonon lifetime, leading to a marked reduction in thermal conductivity. In the second stage (II to III), further crystallization induces ND grains with medium-range order, effectively suppressing phonon scattering and increasing phonon lifetime, resulting in increased thermal conductivities at higher densities.

Notably, the structural evolution of a-DGs is not merely a simple variation in the content of the composite that can be predictable but rather a phase transition process from GC to the ND/DMG composite. This phase transition behavior leads to an innovative anomalous thermal conductivity evolution that has not been observed in other amorphous carbons or amorphous materials. This anomalous trend in thermal conductivity provides a promising strategy for tailoring heat transport in amorphous carbons. Given the exceptional mechanical properties of a-DG and the DMG-ND composite—such as high damping capabilities (45), superhard, ultrastrong, and good conductive (21)—this tunability may hold broad implications for uncovering previously unknown structure-property relationships in vitreous materials and inspiring multifunctional applications including thermal management in microelectronic devices (8, 9, 67) and advanced damping materials (45), where a combination of mechanical robustness and controlled thermal transport is critically required.

Phonon characterization demonstrates that the anomalous thermal conductivity is primarily attributed to the evolution of MFP and phonon lifetime in the medium-frequency range of 7 to 30 THz, rather than heat capacity and phonon group velocity, as the structure transitions from a graphene-like to a diamond-like configuration. This finding is distinctive from all other studies that claimed low-frequency phonons (<10 THz) play a dominant role in thermal conductivity of amorphous carbon (36, 37). The insights obtained here fills the knowledge gap regarding the phase transition pathway from sp^2 -hybridized DMG to sp^3 -hybridized ND and challenges the conventional understanding of monotonically increasing thermal conductivity with density and sp^3 hybridization. Our study explored a relatively tunable transition pathway within this transitional region and provides clearer insights into the critical role of microstructural ordering and phonon lifetimes in determining thermal conductivity in amorphous carbons.

MATERIALS AND METHODS

MD simulations

Large-scale MD simulations were conducted using the large-scale atomic/molecular massively parallel simulator (LAMMPS) (68). The EDIP developed by Marks was used (46), as it effectively describes the physical properties of amorphous carbons. With periodic boundary conditions and a time step of 1 fs, the DGN precursor with a density of 1.0 g cm^{-3} was heated and compressed to evolve into a series of a-DG structures, during which ND grains nucleated and grew within the DMG matrix (45). Given the heterogeneous microstructures and medium-/short-range order in a-DGs, a large simulation box containing a sufficient number of atoms is essential for accurately capturing the statistical characteristics of the complex topologies and overall properties while minimizing structural anisotropies. In fig. S7, a series of a-DG models with different sizes was constructed in our simulations, comprising 16,000, 23,000, 55,000, and 320,000 atoms. All models exhibit consistent sp^3 hybridizations and crystallinities, as shown in fig. S7E. To assess the size effect on structural anisotropies, Zener ratios were calculated from elastic constants (fig. S7D). The Zener ratios for models with 55,000 and 320,000 atoms are closer to 1, indicating markedly improved isotropy, which is considered sufficient for further simulations of thermal conductivities and phonon transport behaviors in subsequent sections.

Homogeneous nonequilibrium molecular dynamic simulations

All results based on NEP were calculated using the graphics processing unit molecular dynamics (GPUMDs) (49). To calculate the thermal conductivity (κ), we used the homogeneous nonequilibrium molecular dynamic (HNEMD) approach (58) for all structures in three directions. The core idea of HNEMD is to use an external driving force to induce a heat current. The thermal conductivity in a given direction can be calculated as follows

$$\kappa(t) = \frac{\langle J_q(t) \rangle_{ne}}{TVF_e} \quad (1)$$

In this context, T represents the temperature, V is the volume, F_e is the driving force at the specified position, and $\langle J_q(t) \rangle_{ne}$ denotes the cumulative average of the heat flux. On the basis of previous work on amorphous carbon and corresponding test results, we set F_e to

0.001, which effectively maintains the stability of our structures. In the above formula, the running thermal conductivity $\kappa(t)$ may exhibit large fluctuations. To obtain a stable thermal conductivity, we use the following definition

$$\kappa(t) = \frac{1}{t} \int_0^t ds \frac{\langle J_q(s) \rangle_{ne}}{TVF_e} \quad (2)$$

HNEMD can be spectrally decomposed in a manner similar to the nonequilibrium molecular dynamics (NEMD) method. Thermal conductivity calculated via HNEMD can be spectrally decomposed, and the steady-state time correlation function $K(t)$ is given by (58)

$$K(t) = \sum_a \sum_{b \neq a} \mathbf{r}_{ab}(0) \left\langle \left(\frac{\partial U_b}{\partial \mathbf{r}_{ba}}(0) \cdot \frac{\mathbf{p}_a(t)}{m_a} \right) \right\rangle_{ne} \quad (3)$$

where \mathbf{r}_{ab} represents the distance vector between particles a and b , U_b represents the potential energy of particle b , \mathbf{p}_a and m_a represents the momentum and mass of particle a . Then, the following Fourier transform is defined

$$\tilde{K}(\omega) = \int_{-\infty}^{\infty} K(t) e^{i\omega t} dt, K(t) = \int_{-\infty}^{\infty} \tilde{K}(\omega) e^{-i\omega t} \frac{d\omega}{2\pi} \quad (4)$$

Spectral heat current (SHC) is then obtained by setting $t = 0$ in the second equation above

$$J_i(\omega) = 2\tilde{K}_i(\omega), \langle J_i \rangle_{ne} = \int_0^{\infty} \frac{d\omega}{2\pi} J_i(\omega) \quad (5)$$

From the SHC, we can easily obtain spectral thermal conductivity

$$\kappa_i(\omega) = \frac{2\tilde{K}_i(\omega)}{TVF_e}, \kappa_i = \int_0^{\infty} \frac{d\omega}{2\pi} \kappa_i(\omega) \quad (6)$$

In the HNEMD calculations, structures containing 55,000 atoms were used, with a box size of approximately 77 \AA by 77 \AA by 77 \AA . All structures exhibited similar thermal conductivity and trends in variation. The structures were relaxed for 200 ps with a 0.5-fs time step under the canonical (NVT) ensemble using the Nosé-Hoover thermostat. Subsequently, thermal conductivity (κ) was calculated in the NVT ensemble with an external driving force for 1 ns, during which κ was confirmed to have converged. The final κ was averaged over three independent ensembles in different directions. The SHC was calculated simultaneously during this process.

The size effect based on HNEMD was checked in fig. S7F, while the simulated results for graphene and diamond confirm the effectiveness of the HNEMD method (fig. S8). Figure S7F illustrates the size effect verification of thermal conductivity, where a-DGs with a density of 2.36 g cm^{-3} , containing 55,000 and 320,000 atoms respectively, exhibit the same thermal conductivities along the x direction. Therefore, a-DG models containing 55,000 atoms were considered to be sufficiently large for subsequent simulations. Besides, we calculated the thermal conductivities of graphene and diamond, finding that the thermal conductivity obtained via the HNEMD method are consistent with previously reported values (65, 69), which validates the effectiveness of HNEMD (fig. S8). Comprehensive results for different directions and model sizes are presented in fig. S5.

Moreover, the thermal conductivity calculated based on HNEMD is classical. Given the assumption of classical statistics and the fact

that room temperature is lower than the Debye temperature for amorphous carbon, the contribution of high-frequency phonons is overestimated. To obtain quantum-corrected thermal conductivity, we can use the following formula to adjust the spectral thermal conductivity and then derive the quantum-corrected thermal conductivity

$$\kappa^q(\omega) = \kappa(\omega) \frac{x^2 e^x}{(e^x - 1)^2} \quad (7)$$

In the formula, $x = \hbar\omega/(k_B T)$, where \hbar is the reduced Planck constant, k_B is the Boltzmann constant, and ω is the phonon frequency. Figure 3A compares the quantum-corrected thermal conductivity with the classical thermal conductivity. After applying the quantum correction, the thermal conductivity decreases by nearly 50%.

NEMD simulations

The NEMD method involves artificially fixing both ends of the simulation box and placing heat sources and cold sources on the left and right sides. By simulating the heat transfer in the middle region of the structure due to these heat sources and applying Fourier's law, the thermal conductivity can be obtained.

To calculate the phonon MFP of the structure, NEMD simulations were performed with NEP, where we still used a size of 77 Å by 77 Å by 77 Å. A periodic boundary along x, y, and z is applied. We evenly divided the model into 21 groups, fixing 2 groups at the left end and setting 8 groups for the heat source and 8 groups for the cold source, and the remaining 3 central groups are used to calculate ballistic thermal conductance $G(\omega)$.

Phonon MFP calculations

The phonon MFP at finite temperature can be derived by combining results from HNEMD and NEMD. The ballistic thermal conductance $G(\omega)$ is calculated using NEMD. Subsequently, the spectral MFP is defined as the ratio of the diffusive spectral thermal conductivity to the ballistic spectral thermal conductance.

$$\lambda(\omega, T) = \frac{\kappa(\omega, T)}{G(\omega)} \quad (8)$$

where ballistic thermal conductance $G(\omega)$ is defined by (48, 70)

$$G(\omega) = \frac{2\tilde{K}(\omega)}{\Delta TV} \quad (9)$$

Group velocity

Typically, group velocity is defined within the context of crystal structures. However, for amorphous structures, the general group velocity can be derived from the current correlation function. In this study, dynasor (63) was used to perform the calculations.

The current correlation density $j(r, t)$ is defined as follows

$$j(r, t) = \sum_i^N v_i(t) \delta[r - r_i(t)] \quad (10)$$

where $v_i(t)$ is the velocity of particle i at time t , which can be split into a longitudinal and transverse part as

$$j_L(q, t) = \sum_i^N [v_i(t) \cdot \hat{q}] \hat{q} e^{iq \cdot r_i(t)} \quad (11)$$

and

$$j_T(q, t) = \sum_i^N \{v_i(t) - [v_i(t) \cdot \hat{q}] \hat{q}\} e^{iq \cdot r_i(t)} \quad (12)$$

Now, the correlation functions can be computed by

$$C_{L,T}(q, t) = \frac{1}{N} \langle j_{L,T}(q, t) \cdot j_{L,T}(-q, 0) \rangle \quad (13)$$

Next, we transform $C_{L,T}$ from the time domain to the frequency domain, using q and ω as the axes, and use a color bar to represent the values of $C_{L,T}$. The group velocity at low frequencies can be approximated as the ratio of ω to the wave vector q through linear fitting (fig. S9).

Volumetric heat capacity

The Debye model was used to calculate volumetric heat capacity.

$$C_V = \left(\frac{\partial \bar{E}}{\partial T} \right)_V = \sum_{j=1}^{3p} \left[\int_0^{\omega_m} g(\omega) d\omega k_B \left(\frac{\hbar\omega}{k_B T} \right)^2 \frac{\exp\left(\frac{\hbar\omega}{k_B T}\right)}{\left[\exp\left(\frac{\hbar\omega}{k_B T}\right) - 1 \right]^2} \right] \quad (14)$$

Here, $g(\omega)$ represents the PDOS, which can be calculated using GPUMD. The cutoff frequency ω_m can be simultaneously determined during the computation of the PDOS.

Supplementary Materials

This PDF file includes:

Figs. S1 to S10

REFERENCES AND NOTES

- Y. Gogotsi, Not just graphene: The wonderful world of carbon and related nanomaterials. *MRS Bull.* **40**, 1110–1121 (2015).
- P. Nemeth, K. McCol, L. A. J. Garvie, C. G. Salzmann, M. Murri, P. F. McMillan, Complex nanostructures in diamond. *Nat. Mater.* **19**, 1126–1131 (2020).
- M.-W. Wang, W. Fan, X. Li, Y. Liu, Z. Li, W. Jiang, J. Wu, Z. Wang, Molecular carbons: How far can we go? *ACS Nano* **17**, 20734–20752 (2023).
- Y. B. Zhu, Z. Y. Fang, Z. T. Zhang, H. A. Wu, Discontinuous phase diagram of amorphous carbons. *Natl. Sci. Rev.* **11**, nwae051 (2024).
- W. J. Joo, J. H. Lee, Y. Jang, S. G. Kang, Y. N. Kwon, J. Chung, S. Lee, C. Kim, T. H. Kim, C. W. Yang, U. J. Kim, B. L. Choi, D. Whang, S. W. Hwang, Realization of continuous Zachariasen carbon monolayer. *Sci. Adv.* **3**, e1601821 (2017).
- L. X. Hou, X. P. Cui, B. Guan, S. Z. Wang, R. A. Li, Y. Q. Liu, D. B. Zhu, J. Zheng, Synthesis of a monolayer fullerene network. *Nature* **606**, 507–510 (2022).
- C. T. Toh, H. J. Zhang, J. H. Lin, A. S. Mayorov, Y. P. Wang, C. M. Orofeo, D. B. Ferry, H. Andersen, N. Kakenov, Z. L. Guo, I. H. Abidi, H. Sims, K. Suenaga, S. T. Pantelides, B. Ozyilmaz, Synthesis and properties of free-standing monolayer amorphous carbon. *Nature* **577**, 199–203 (2020).
- H. Tian, Y. Ma, Z. Li, M. Cheng, S. Ning, E. Han, M. Xu, P. F. Zhang, K. Zhao, R. Li, Y. Zou, P. Liao, S. Yu, X. Li, J. Wang, S. Liu, Y. Li, X. Huang, Z. Yao, D. Ding, J. Guo, Y. Huang, J. Lu, Y. Han, Z. Wang, Z. G. Cheng, J. Liu, Z. Xu, K. Liu, P. Gao, Y. Jiang, L. Lin, X. Zhao, L. Wang, X. Bai, W. Fu, J. Y. Wang, M. Li, T. Lei, Y. Zhang, Y. Hou, J. Pei, S. J. Pennycook, E. Wang, J. Chen, W. Zhou, L. Liu, Disorder-tuned conductivity in amorphous monolayer carbon. *Nature* **615**, 56–61 (2023).
- H. Tian, Z. Yao, Z. Li, J. Guo, L. Liu, Unlocking more potentials in two-dimensional space: Disorder engineering in two-dimensional amorphous carbon. *ACS Nano* **17**, 24468–24478 (2023).
- Y. Lin, L. Zhang, H. K. Mao, P. Chow, Y. M. Xiao, M. Baldini, J. F. Shu, W. L. Mao, Amorphous diamond: A high-pressure superhard carbon allotrope. *Phys. Rev. Lett.* **107**, 175504 (2011).
- M. Hu, J. L. He, Z. S. Zhao, T. A. Strobel, W. T. Hu, D. L. Yu, H. Sun, L. Y. Liu, Z. H. Li, M. D. Ma, Y. Kono, J. F. Shu, H. K. Mao, Y. W. Fei, G. Y. Shen, Y. B. Wang, S. J. Juhl, J. Y. Huang, Z. Y. Liu, B. Xu, Y. J. Tian, Compressed glassy carbon: An ultrastrong and elastic interpenetrating graphene network. *Sci. Adv.* **3**, e1603213 (2017).
- S. S. Zhang, Z. H. Li, K. Luo, J. L. He, Y. F. Gao, A. V. Soldatov, V. Benavides, K. Y. Shi, A. M. Nie, B. Zhang, W. T. Hu, M. D. Ma, Y. Liu, B. Wen, G. Y. Gao, B. Liu, Y. Zhang, Y. Shu, D. L. Yu, X. F. Zhou, Z. S. Zhao, B. Xu, L. Su, G. Q. Yang, O. P. Chernogorova, Y. J. Tian, Discovery of carbon-based strongest and hardest amorphous material. *Natl. Sci. Rev.* **9**, nwab140 (2022).

13. Y. C. Wang, Y. B. Zhu, H. A. Wu, Formation and topological structure of three-dimensional disordered graphene networks. *Phys. Chem. Chem. Phys.* **23**, 10290–10302 (2021).
14. Y. Feng, D. J. Davidson, W. Sun, V. Milani, G. W. Howieson, N. J. Westwood, W. Zhou, Formation of nanodiamonds during pyrolysis of butanosolv lignin. *ACS Nano* **18**, 24803–24811 (2024).
15. H. Gou, Microstructural landscape of amorphous carbon. *Natl. Sci. Rev.* **11**, nwae125 (2024).
16. A. San-Miguel, How to make macroscale non-crystalline diamonds. *Nature* **599**, 563–564 (2021).
17. F. Pan, K. Ni, T. Xu, H. Chen, Y. Wang, K. Gong, C. Liu, X. Li, M.-L. Lin, S. Li, X. Wang, W. Yan, W. Yin, P.-H. Tan, L. Sun, D. Yu, R. S. Ruoff, Y. Zhu, Long-range ordered porous carbons produced from C₆₀. *Nature* **614**, 95–101 (2023).
18. H. Tang, X. H. Yuan, Y. Cheng, H. Z. Fei, F. Y. Liu, T. Liang, Z. D. Zeng, T. Ishii, M. S. Wang, T. Katsura, H. W. Sheng, H. Y. Gou, Synthesis of paracrystalline diamond. *Nature* **599**, 605–610 (2021).
19. Z. Zeng, L. Yang, Q. Zeng, H. Lou, H. Sheng, J. Wen, D. J. Miller, Y. Meng, W. Yang, W. L. Mao, H. K. Mao, Synthesis of quenchable amorphous diamond. *Nat. Commun.* **8**, 322 (2017).
20. Y. C. Shang, Z. D. Liu, J. J. Dong, M. G. Yao, Z. X. Yang, Q. J. Li, C. G. Zhai, F. R. Shen, X. Y. Hou, L. Wang, N. Q. Zhang, W. Zhang, R. Fu, J. F. Ji, X. M. Zhang, H. Lin, Y. W. Fei, B. Sundqvist, W. H. Wang, B. B. Liu, Ultrahard bulk amorphous carbon from collapsed fullerene. *Nature* **599**, 599–604 (2021).
21. Z. H. Li, Y. J. Wang, M. D. Ma, H. C. Ma, W. T. Hu, X. Zhang, Z. W. Zhuge, S. S. Zhang, K. Luo, Y. F. Gao, L. Sun, A. V. Soldatov, Y. J. Wu, B. Liu, B. Z. Li, P. Ying, Y. Zhang, B. Xu, J. L. He, D. L. Yu, Z. Y. Liu, Z. S. Zhao, Y. Z. Yue, Y. J. Tian, X. Y. Li, Ultrastrong conductive in situ composite composed of nanodiamond incoherently embedded in disordered multilayer graphene. *Nat. Mater.* **22**, 42–49 (2023).
22. Y. Shang, M. Yao, Z. Liu, R. Fu, L. Yan, L. Yang, Z. Zhang, J. Dong, C. Zhai, X. Hou, L. Fei, G. Zhang, J. Ji, J. Zhu, H. Lin, B. Sundqvist, B. Liu, Enhancement of short/medium-range order and thermal conductivity in ultrahard sp³ amorphous carbon by C70 precursor. *Nat. Commun.* **14**, 7860 (2023).
23. M. Chen, Y. Zhu, J. Xia, H. Wu, Molecular insights into the initial formation of pyrolytic carbon upon carbon fiber surface. *Carbon* **148**, 307–316 (2019).
24. P. Nemeth, K. McColl, R. L. Smith, M. Murri, L. A. J. Garvie, M. Alvaro, B. Pecz, A. P. Jones, F. Cora, C. G. Salzmann, P. F. McMillan, Diamond-graphene composite nanostructures. *Nano Lett.* **20**, 3611–3619 (2020).
25. A. Dernov, M. Kowalik, A. C. T. van Duin, T. Dumitrică, Mapping the structural–mechanical landscape of amorphous carbon with ReaxFF molecular dynamics. *J. Appl. Phys.* **137**, 065107 (2025).
26. X. Zhang, L. Zhong, A. Mateos, A. Kudo, A. Vyatskikh, H. J. Gao, J. R. Greer, X. Y. Li, Theoretical strength and rubber-like behaviour in micro-sized pyrolytic carbon. *Nat. Nanotechnol.* **14**, 762–769 (2019).
27. Y. B. Zhu, Y. C. Wang, B. Wu, Z. Z. He, J. Xia, H. A. Wu, Micromechanical landscape of three-dimensional disordered graphene networks. *Nano Lett.* **21**, 8401–8408 (2021).
28. K. Luo, B. Liu, W. T. Hu, X. Dong, Y. B. Wang, Q. Huang, Y. F. Gao, L. Sun, Z. S. Zhao, Y. J. Wu, Y. Zhang, M. D. Ma, X. F. Zhou, J. L. He, D. L. Yu, Z. Y. Liu, B. Xu, Y. J. Tian, Coherent interfaces govern direct transformation from graphite to diamond. *Nature* **607**, 486–491 (2022).
29. D. R. McKenzie, D. Muller, B. A. Pailthorpe, Compressive-stress-induced formation of thin-film tetrahedral amorphous carbon. *Phys. Rev. Lett.* **67**, 773–776 (1991).
30. N. A. Marks, D. R. McKenzie, B. A. Pailthorpe, M. Bernasconi, M. Parrinello, Microscopic structure of tetrahedral amorphous carbon. *Phys. Rev. Lett.* **76**, 768–771 (1996).
31. G. Galli, R. M. Martin, R. Car, M. Parrinello, Structural and electronic properties of amorphous carbon. *Phys. Rev. Lett.* **62**, 555–558 (1989).
32. Z. T. Zhang, Z. Y. Fang, H. A. Wu, Y. B. Zhu, Temperature-dependent paracrystalline nucleation in atomically disordered diamonds. *Nano Lett.* **24**, 312–318 (2024).
33. A. A. Balandin, Thermal properties of graphene and nanostructured carbon materials. *Nat. Mater.* **10**, 569–581 (2011).
34. I. Suarez-Martinez, N. A. Marks, Effect of microstructure on the thermal conductivity of disordered carbon. *Appl. Phys. Lett.* **99**, 033101 (2011).
35. A. Giri, C. J. Dionne, P. E. Hopkins, Atomic coordination dictates vibrational characteristics and thermal conductivity in amorphous carbon. *NPI Comput. Mater.* **8**, 55 (2022).
36. J. Moon, Z. Tian, Crystal-like thermal transport in amorphous carbon. *arXiv:2405.07298 [cond-mat.dis-nn]* (2024).
37. Y. Wang, Z. Fan, P. Qian, M. A. Caro, T. Ala-Nissila, Density dependence of thermal conductivity in nanoporous and amorphous carbon with machine-learned molecular dynamics. *Phys. Rev. B* **111**, 094205 (2025).
38. A. J. Bullen, K. E. O'Hara, D. G. Cahill, O. Monteiro, A. von Keudell, Thermal conductivity of amorphous carbon thin films. *J. Appl. Phys.* **88**, 6317–6320 (2000).
39. C. J. Morath, H. J. Maris, J. J. Cuomo, D. L. Pappas, A. Grill, V. V. Patel, J. P. Doyle, K. L. Saenger, Picosecond optical studies of amorphous diamond and diamondlike carbon: Thermal conductivity and longitudinal sound velocity. *J. Appl. Phys.* **76**, 2636–2640 (1994).
40. G. Chen, P. Hui, S. Xu, Thermal conduction in metalized tetrahedral amorphous carbon (ta-C) films on silicon. *Thin Solid Films* **366**, 95–99 (2000).
41. M. Shamsa, W. L. Liu, A. A. Balandin, C. Casiraghi, W. I. Milne, A. C. Ferrari, Thermal conductivity of diamond-like carbon films. *Appl. Phys. Lett.* **89**, 161921 (2006).
42. W. Hurler, M. Pietralla, A. Hammerschmidt, Determination of thermal properties of hydrogenated amorphous carbon thin films via mirage effect measurement. *Diamond Relat. Mater.* **4**, 954–957 (1995).
43. G. A. Slack, Anisotropic thermal conductivity of pyrolytic graphite. *Phys. Rev.* **127**, 694–701 (1962).
44. R. Thapa, C. Ugumadu, K. Nepal, J. Tremblay, D. A. Drabold, Ab initio simulation of amorphous graphite. *Phys. Rev. Lett.* **128**, 236402 (2022).
45. Z. Zhang, H. Wu, Y. Zhu, Simultaneously enhanced damping and stiffness of amorphous diaphite. *ACS Nano* **18**, 34312–34321 (2024).
46. N. A. Marks, Generalizing the environment-dependent interaction potential for carbon. *Phys. Rev. B* **63**, 035401 (2000).
47. K. Song, R. Zhao, J. Liu, Y. Wang, E. Lindgren, Y. Wang, S. Chen, K. Xu, T. Liang, P. Ying, N. Xu, Z. Zhao, J. Shi, J. Wang, S. Lyu, Z. Zeng, S. Liang, H. Dong, L. Sun, Y. Chen, Z. Zhang, W. Guo, P. Qian, J. Sun, P. Erhart, T. Ala-Nissila, Y. Su, Z. Fan, General-purpose machine-learned potential for 16 elemental metals and their alloys. *Nat. Commun.* **15**, 10208 (2024).
48. P. Ying, C. Qian, R. Zhao, Y. Wang, K. Xu, F. Ding, S. Chen, Z. Fan, Advances in modeling complex materials: The rise of neuroevolution potentials. *Chem. Phys. Rev.* **6**, 011310 (2025).
49. Z. Fan, Y. Wang, P. Ying, K. Song, J. Wang, Y. Wang, Z. Zeng, K. Xu, E. Lindgren, J. M. Rahm, A. J. Gabourie, J. Liu, H. Dong, J. Wu, Y. Chen, Z. Zhong, J. Sun, P. Erhart, Y. Su, T. Ala-Nissila, GPUMD: A package for constructing accurate machine-learned potentials and performing highly efficient atomistic simulations. *J. Chem. Phys.* **157**, 114801 (2022).
50. J. Shi, Z. Liang, J. Wang, S. Pan, C. Ding, Y. Wang, H. T. Wang, D. Xing, J. Sun, Double-shock compression pathways from diamond to BC8 carbon. *Phys. Rev. Lett.* **131**, 146101 (2023).
51. X. Zhou, Y. Liu, B. Tang, J. Wang, H. Dong, X. Xiu, S. Chen, Z. Fan, Million-atom heat transport simulations of polycrystalline graphene approaching first-principles accuracy enabled by neuroevolution potential on desktop GPUs. *J. Appl. Phys.* **137**, 014305 (2025).
52. E. Pop, V. Varshney, A. K. Roy, Thermal properties of graphene: Fundamentals and applications. *MRS Bull.* **37**, 1273–1281 (2012).
53. C. Moelle, M. Werner, F. Szűcs, D. Wittorf, M. Sellschopp, J. von Borany, H. J. Fecht, C. Johnston, Specific heat of single-, poly- and nanocrystalline diamond. *Diamond Relat. Mater.* **7**, 499–503 (1998).
54. M. Schwoerer-Böhning, A. T. Macrander, D. A. Arms, Phonon dispersion of diamond measured by inelastic x-ray scattering. *Phys. Rev. Lett.* **80**, 5572–5575 (1998).
55. J. Kulda, H. Kainzmaier, D. Strauch, B. Dörner, M. Lorenzen, M. Krisch, Overbending of the longitudinal optical phonon branch in diamond as evidenced by inelastic neutron and x-ray scattering. *Phys. Rev. B* **66**, 241202 (2002).
56. M. Mohr, J. Maultzsch, E. Dobardžić, S. Reich, I. Milošević, M. Damnjanović, A. Bosak, M. Krisch, C. Thomsen, Phonon dispersion of graphite by inelastic x-ray scattering. *Phys. Rev. B* **76**, 035439 (2007).
57. L. Wirtz, A. Rubio, The phonon dispersion of graphite revisited. *Solid State Commun.* **131**, 141–152 (2004).
58. Z. Fan, H. Dong, A. Harju, T. Ala-Nissila, Homogeneous nonequilibrium molecular dynamics method for heat transport and spectral decomposition with many-body potentials. *Phys. Rev. B* **99**, 064308 (2019).
59. A. J. Gabourie, Z. Fan, T. Ala-Nissila, E. Pop, Spectral decomposition of thermal conductivity: Comparing velocity decomposition methods in homogeneous molecular dynamics simulations. *Phys. Rev. B* **103**, 205421 (2021).
60. Y. Wang, Z. Fan, P. Qian, M. A. Caro, T. Ala-Nissila, Quantum-corrected thickness-dependent thermal conductivity in amorphous silicon predicted by machine learning molecular dynamics simulations. *Phys. Rev. B* **107**, 054303 (2023).
61. X. Wu, Y. Wu, X. Huang, Z. Fan, S. Volz, Q. Han, M. Nomura, Isotope interface engineering for thermal transport suppression in cryogenic graphene. *Mater. Today Phys.* **46**, 101500 (2024).
62. J. Moon, B. Latour, A. J. Minnich, Propagating elastic vibrations dominate thermal conduction in amorphous silicon. *Phys. Rev. B* **97**, 024201 (2018).
63. E. Fransson, M. Slabanja, P. Erhart, G. Wahnström, dynasor—A tool for extracting dynamical structure factors and current correlation functions from molecular dynamics simulations. *Adv. Theor. Simul.* **4**, 2000240 (2021).
64. C. Lu, Z.-H. Li, S. Li, Z. Li, Y. Zhang, J. Zhao, N. Wei, Molecular dynamics study of thermal transport properties across covalently bonded graphite-nanodiamond interfaces. *Carbon* **213**, 118250 (2023).
65. A. Ward, D. A. Broido, D. A. Stewart, G. Deinzer, Ab initio theory of the lattice thermal conductivity in diamond. *Phys. Rev. B* **80**, 125203 (2009).
66. W. A. Diery, E. A. Moujaes, R. W. Nunes, Nature of localized phonon modes of tilt grain boundaries in graphene. *Carbon* **140**, 250–258 (2018).
67. P. Liao, H. Guo, H. Niu, R. Li, G. Yin, L. Kang, L. Ren, R. Lv, H. Tian, S. Liu, Z. Yao, Z. Li, Y. Wang, L. Yang Zhang, U. Sasaki, W. Li, Y. Luo, J. Guo, Z. Xu, L. Wang, R. Zou, S. Bai, L. Liu, Core-shell

- engineered fillers overcome the electrical-thermal conductance trade-Off. *ACS Nano* **18**, 30593–30604 (2024).
68. S. Plimpton, Fast parallel algorithms for short-range molecular dynamics. *J. Comput. Phys.* **117**, –19 (1995).
69. Z. Han, X. Ruan, Thermal conductivity of monolayer graphene: Convergent and lower than diamond. *Phys. Rev. B* **108**, L121412 (2023).
70. Z. Li, S. Xiong, C. Sievers, Y. Hu, Z. Fan, N. Wei, H. Bao, S. Chen, D. Donadio, T. Ala-Nissila, Influence of thermostatting on nonequilibrium molecular dynamics simulations of heat conduction in solids. *J. Chem. Phys.* **151**, 234105 (2019).

Acknowledgments: We thank N. A. Marks at Curtin University for providing the EDIP force file. The numerical calculations were performed on the supercomputing system in Hefei Advanced Computing Center and the Supercomputing Center of University of Science and Technology of China. **Funding:** This work was jointly supported by the National Natural Science Foundation of China 12388101 (H.W.), 12232016 (H.W.), and 12172346 (Y.Z.), the National Key Research and

Development Program of China 2024YFA1211700 (Y.Z.), the Youth Innovation Promotion Association CAS 2022465 (Y.Z.), the USTC Tang Scholar, the Fundamental Research Funds for the Central Universities WK2090000087 (H.W.), and the opening fund of State Key Laboratory of Nonlinear Mechanics. H.M. thanks the funding support from the University of Science and Technology of China (USTC) Startup Program KY2090000117 (H.M.). **Author contributions:** Y.Z. and H.M. conceived the idea and designed the research. H.W. supervised the project. Z.Z. and J.L. performed the simulations. Z.Z., J.L., H.M., and Y.Z. analyzed the data and wrote the paper. **Competing interests:** The authors declare that they have no competing interests. **Data and materials availability:** All data needed to evaluate the conclusions in the paper are present in the paper and/or the Supplementary Materials.

Submitted 17 March 2025

Accepted 1 May 2025

Published 6 June 2025

10.1126/sciadv.adx5007